Very high order finite volume solver for multi component two-phase flow with phase change using a posteriori Multi Optimal Order Detection

Michael Deligant[a,*], Carlos Romero[a], Xesus Nogueira[b], Luis Ramirez[b], Mathieu Specklin[a], Farid Bakir[a], Sofiane Khelladi[a]

[a]*Arts et Metiers Institute of Technology, CNAM, LIFSE, HESAM University, F-75013 Paris, France*
[b]*Group of Numerical Methods in Engineering-GMNI, Center for Technological Innovation in Construction and Civil Engineering-CITEEC, Universidade da Coruña, Civil Engineering School, Campus de Elviña, 15071, A Coruña, Spain*

Abstract

In this work we propose a very high-order compressible finite volume scheme with a posteriori stabilization for the computation of multi-component two-phase flow with phase change. It is based on finite volume approach using moving least square reproducing kernels for high order reconstructions. It is also coupled with multi optimal order detection (MOOD) to get high accuracy low dissipation scheme while maintaining boundedness and preventing numerical oscillations at interfaces and strong gradient zones. The properties of the proposed framework are demonstrated on classical test problems starting with convergence order verification on simple scalar advection test cases. More complex shock and more stringent tubes tests with various water, steam and air concentration are then simulated and compared with available reference in the literature. Finally the ability of the proposed approach is illustrated with the simulation of a liquid oxygen jet in gaseous hydrogen. The results features vortices, mixing and evaporation at the liquid/vapor interface.

Keywords: two-phase flow, Homogeneous Relaxation Model, a posteriori, Multi Optimal Order detection, MOOD

1. Introduction

In computational fluid dynamics, accurate simulations of multiphase flows are still very challenging, particulary in presence of phase transitions [1] and multi-component flows [2]. These complex two-phase flows with phase transition are encountered in a large range of industrial applications such as nuclear energy [3, 4], cryogenic tanks [5, 6] for space propulsion, energy storage or carbon capture and sequestration [7]. Advance numerical model are required to accurately simulate these problems.

Various numerical approaches are adapted to deal with two-phase flow. Smooth Particle Hydrodynamics (SPH) approach are usually well suited for incompressible or weakly-compressible flows and with free surface [8–10]. Lattice Boltzmann simulates fluid behavior at the mesoscale and easily handle complex interfaces [11–13]. Mesh-based methods like the finite volume approach offers a robust and flexible framework for simulating two-phase flows, especially on complex geometries. Finite volume approach in particular is considered a good choice for its conservative properties. In this framework, phase separation can be achieved either with diffuse or a sharp interface methods. In the sharp-interface models, the phases are treated separately and there is a discontinuity between them, at the interface. In these methods there is a need to track the interface. Diffuse interface methods offer multiple advantages in modeling two-phase flows, but they require careful implementation and the use of adapted solvers to ensure that the interface remains sharp enough, and well-defined throughout the simulation. But they often involves a combination of high-resolution schemes[14, 15], interface sharpening algorithms[16], and possibly mesh refinement techniques[17].

In this work, we propose using the finite volume method with a diffuse interface on an unstructured mesh to handle multi-component two-phase flows. The finite volume approach offers the advantage of being conservative, while the

*Corresponding author. Tel.: +33-1-44-24-63-45
Email address: michael.deligant@ensam.eu (Michael Deligant)

diffuse interface eliminates the need for special treatments or reconstructions. The use of unstructured mesh allows to deal with any complex geometries that can be encountered in industrial applications [18].

High-order methods are generally employed to get accurate results with limited mesh refinement. They also contribute in reducing the interface diffusion due to their low diffusivity properties. However, a drawback of high-order methods is the numerical instabilities they generate when encountering strong gradients, particularly at two-phase interfaces or in the presence of shocks. Typically, this issue is mitigated using slope limiters during the flux reconstruction step[19, 20]. Classical limiters, acting a priori, tend to introduce unnecessary dissipation in areas of smooth flow. To address this problem, we use the Multi Optimal Order Detection (MOOD) approach [21–23], acting a posteriori, to maintain the targeted order while preventing numerical oscillations [24] as much as possible. MOOD also contribute in preserving the boundedness of the mass fraction which is fundamental to prevent non-physical results. Multiphase flows also exhibit a wide range of Mach numbers due to significant variations in the speed of sound. Therefore, a compressible solver capable of handling this constraint is essential. This generally dealt with low Mach pre-conditioned solvers [25] or all-speed capable solvers [26].

In this work we propose a high-order finite volume scheme with a posteriori stabilization for the computation of multi-species flow with phase change. To address multi-component two-phase flows, we adopt the solver framework proposed by Saurel et al [27] and further developed by Chiapolino et al [28]. Using the temperature-pressure equilibrium with the Homogeneous Relaxation Model (HRM), the system is reduced to four equations (in 1D for a single component). The Noble-Abel Stiffened Gas (NASG) Equation of State [29, 30] is used. It preserves the hyperbolicity of the system, allowing for arbitrary density jumps at interfaces and arbitrary flow speeds. We use a conservative formulation that employs mass fraction transport. Phase transition modelling relies on Gibbs free energy relaxation.

The paper is organized as follows. Section 2 introduces the governing equations of the two-phase flow solver. Section 3 presents the numerical methods, namely the FV-MLS+MOOD framework. Section 4 gathers numerical test cases showing the capabilities of the proposed method to address various simulation challenges. The final section summarizes the work and presents the conclusions and perspectives.

2. Governing equations

The physical approach considered in this work is based on the reduced four-equation model for two fluids (proposed by Saurel and coworkers [27]) extended with an extra mass balance equation for modelling a multicomponent gas mixture [28]. In this approach it is considered that each gas constituent occupies its own volume at the pressure and temperature of equilibrium. Therefore, in [28], it was demonstrated that this is equivalent to consider the gas phase as an ideal mixture following the Dalton's law. Thus, the governing equations for the extended-model take the conservative form below,

$$
\begin{aligned}
&\frac{\partial \rho}{\partial t} + \nabla \cdot (\rho \vec{u}) = 0 \\
&\frac{\partial \rho \vec{u}}{\partial t} + \nabla \cdot \left(\rho \vec{u} \otimes \vec{u} + P \underline{\underline{I}} \right) = 0 \\
&\frac{\partial \rho E}{\partial t} + \nabla \cdot ((\rho E + P) \vec{u}) = 0 \\
&\frac{\partial \rho Y_1}{\partial t} + \nabla \cdot (\rho Y_1 \vec{u}) = \rho \nu \, (g_2 - g_1) \\
&\frac{\partial \rho Y_k}{\partial t} + \nabla \cdot (\rho Y_k \vec{u}) = 0
\end{aligned}
\tag{1}
$$

where k corresponding to the k-th non condensable gas component and g_j (with j=1,2) denotes the Gibbs free energy of the j phase. The parameter $\nu(A_I, T, p)$ is the relaxation parameter which controls the thermodynamic equilibrium rate, being a function of the interfacial area, the pressure and the temperature. When phase transition occurs at the interface between a liquid and its vapor, local thermodynamic equilibrium is assumed. In this framework, two

methodologies for phase transition are presented in this work. In both, the relaxation parameter is considered big enough ($\nu \longrightarrow \infty$) so the thermodynamic equilibrium is reached immediately (stiff relaxation) [31]. This means that pure phases are allowed to have any temperature and pressure, but, since there is a mixture zone, they reach instantaneously equilibrium. The evolution to the equilibrium state is considered at constant energy and specific volume. Hence, pressure and temperature change with a new distribution of the mass fractions.

The total energy of the system is defined as,

$$E = e + \frac{1}{2}\vec{u}\vec{u} \tag{2}$$

Now, the mixture equations for the thermodynamic closure are defined as,

$$\begin{cases} T = T_k \\ p = p_k \\ e = \sum_{k=1}^{N} Y_k e_k \\ \nu = \sum_{k=1}^{N} Y_k \nu_k \end{cases} \tag{3}$$

Concerning the equation of state, each pure phase is assumed to follow the NASG-EOS (Equation 4), which requires the definition of 6 parameters ($c_{v,k}$, γ_k, $p_{\infty,k}$, q_k, q'_k, b_k) Here, all the gaseous phases (k=2,...,N) are considered as ideal gases, which means $p_{\infty,k} = 0$, $b_k = 0$.

$$\begin{cases} p_k(\rho_k, e_k) = \dfrac{\rho_k(\gamma_k - 1)(e_k - q_k)}{1 - \rho_k b_k} - \gamma_k p_{\infty,k} \\ T_k(p_k, \rho_k) = \dfrac{(p_k + p_{\infty,k})(1 - \rho_k b_k)}{\rho_k c_{v,k}(\gamma_k - 1)} \\ \upsilon_k(p_k, T_k) = \dfrac{(\gamma_k - 1)c_{v,k}T_k}{p + p_{\infty,k}} + b_k \\ h_k(p_k, T_k) = \gamma_k c_{v,k} T_k + b_k p_k + q_k \\ g_k(p_k, T_k) = (\gamma_k c_{v,k} - q'_k)T_k - c_{v,k}T_k ln\left(\dfrac{T_k^{\gamma_k}}{(p_k + p_{\infty,k})^{\gamma_k - 1}}\right) + b_k p_k + q_k \\ c_k(p_k, \rho_k) = \sqrt{\gamma_k \dfrac{p_k + p_{\infty,k}}{\rho_k (1 - \rho_k b_k)}} \end{cases} \tag{4}$$

Concerning the mixture speed of sound, the mechanical equilibrium sound speed based on the Wood's formulation is adopted due to its better stability and simplicity, reading,

$$c_W = \frac{1}{\sqrt{\rho\left(\dfrac{\alpha_1}{\rho_1 c_1^2} + \dfrac{\alpha_2}{\rho_2 c_2^2} + \dfrac{\alpha_3}{\rho_3 c_3^2}\right)}}$$

with $\alpha_k = \frac{Y_k \rho}{\rho_k}$ the volume fraction of the k component.

3. Numerical method

The two-dimensional homogeneous relaxation model of equilibrium given by equation (1) can be written in two-dimensional conservative form as :

$$\frac{\partial \mathbf{U}}{\partial t} + \frac{\partial (\mathbf{F}_x(\mathbf{U}))}{\partial x} + \frac{\partial (\mathbf{F}_y(\mathbf{U}))}{\partial y} = \mathbf{0} \tag{5}$$

where the conserved variables are,

$$\mathbf{U} = \begin{pmatrix} \rho \\ \rho u \\ \rho v \\ \rho E \\ \rho Y_1 \\ \rho Y_3 \end{pmatrix}$$

being ρ the density, Y_1 the liquid mass fraction, Y_3 the mass fraction of non condensable phase, ρu and ρv the x- and y- directional momentum and E the total energy. The vapor mass fraction Y_2 is deduced from $Y_1 + Y_2 + Y_3 = 1$.

The inviscid fluxes are defined as follows,

$$\mathbf{F}_x(\mathbf{U}) = \begin{pmatrix} \rho u \\ \rho u^2 + p \\ \rho uv \\ (\rho E + p)u \\ \rho Y_1 u \\ \rho Y_3 u \end{pmatrix}, \mathbf{F}_y(\mathbf{U}) = \begin{pmatrix} \rho v \\ \rho uv \\ \rho v^2 + p \\ (\rho E + p)v \\ \rho Y_1 v \\ \rho Y_3 v \end{pmatrix}.$$

Equation (5) can be written in semi-discrete form using the Finite Volume Methods as

$$\int_{\Omega_I} \frac{\partial \boldsymbol{U}}{\partial t} \, d\Omega + \int_{\Gamma_I} \boldsymbol{\Theta}(\boldsymbol{U}^{hb+}, \boldsymbol{U}^{hb-}) \, d\Gamma = \mathbf{0} \tag{6}$$

where $\boldsymbol{\Theta}(\boldsymbol{U}^{hb+}, \boldsymbol{U}^{hb-})$ is a suitable numerical flux, and + and − refers to the left and right Riemann states of the cell I. In this work, the Riemann states are obtained using Taylor expansions and Moving Least Squares to calculate the derivatives. Also, HLLC [32–34] approximate Riemann solver is used for its ability to deal with various Mach numbers as in [1, 28, 35].

3.1. Moving Least Squares approximations

In the present work, high-order is achieved by using Taylor expansions to compute the Riemann states at the interfaces, and using Moving Least Squares (MLS) approximations for the computation of the derivatives required in the Taylor reconstruction. This approach is extensively described in [26, 36–39]. Here we only introduce a brief description of the computation procedure.

In brief, a Moving Least Squares approximation of a function Φ belongs to the subspace spanned by a set of *basis functions* $\{N_I(\boldsymbol{x})\}$ associated to the nodes, such that it is given by

$$\boldsymbol{\Phi}^{MLS}(\boldsymbol{x}) = \sum_{j=1}^{n_{\boldsymbol{x}}} N_j(\boldsymbol{x}) \boldsymbol{\Phi}_j \tag{7}$$

which states that the approximation at a point $\boldsymbol{x}$ is computed using certain $n_{\boldsymbol{x}}$ surrounding nodes. This set of nodes is referred to as the *stencil* associated to the evaluation point $\boldsymbol{x}$. The number of nodes of the stencil depends on the order of the reconstruction [26, 37, 38].

In equation (7) $N_j(\boldsymbol{x})$ are the MLS shape functions. To compute them, we define an m-dimensional basis, which in this case is defined as a polynomial basis $\boldsymbol{p}^T(\boldsymbol{x}) = (1, x, y, x^2, y^2, xy, ...) \in \mathbb{R}^m$. The dimension of the basis, m, determines the minimum number of points of the stencil. However, for stability reasons, this minimum number should be increased. For example for cubic basis, we used $n_{\boldsymbol{x}} = 20$ cells in the stencils.

Then, the MLS-shape functions are defined as

$$\boldsymbol{N}^T(\boldsymbol{x}) = \boldsymbol{p}^T(\boldsymbol{x})\boldsymbol{M}^{-1}(\boldsymbol{x})\boldsymbol{P}(\boldsymbol{x})\boldsymbol{W}(\boldsymbol{x})$$

where $\boldsymbol{P} = [\boldsymbol{p}^T(\boldsymbol{x_j})]_j$, is a $m \times n_{\boldsymbol{x}}$ matrix where the basis functions are evaluated at each point of the stencil, and $\boldsymbol{M}(\boldsymbol{x})$ is the $m \times m$ moment matrix given by

$$\boldsymbol{M}(\boldsymbol{x}) = \boldsymbol{P}(\boldsymbol{x})\boldsymbol{W}(\boldsymbol{x})\boldsymbol{P}^T(\boldsymbol{x})$$

The kernel function $\boldsymbol{W}$ determines the properties of the scheme, required in the computation of $\boldsymbol{N}^T(\boldsymbol{x})$. We have chosen to use an exponential kernel [39], defined as :

$$W(x, x^*, \kappa_x) = \frac{e^{-\left(\frac{s}{2c}\right)^2} - e^{-\kappa^2}}{1 - e^{-\kappa^2}}$$

with $s = \left|x_j - x^*\right|$, $d_m = max\left(\left|x_j - x^*\right|\right)$, with $j = 1, \ldots, n_{x^*}$, $c = \frac{d_m}{\kappa}$, x is the position of every cell centroid of the stencil and κ is a shape parameter, which is this work is taken as $\kappa = 6$. Moreover, x^* refers to the position of the point where the MLS shape function is evaluated.

In order to reconstruct the variable at integration points, we use Taylor series expansions. Thus, to define a quadratic reconstruction inside cell I, we require the computation of first and second derivatives

$$\boldsymbol{U}_I^{hb}(\boldsymbol{x}) = \boldsymbol{U}_I^h + \boldsymbol{\nabla U}_I^h \cdot (\boldsymbol{x} - \boldsymbol{x}_I) + \frac{1}{2}(\boldsymbol{x} - \boldsymbol{x}_I)^T \boldsymbol{H}^h (\boldsymbol{x} - \boldsymbol{x}_I)$$

These derivatives are computed at the cell centroids using MLS, from the derivatives of the shape functions as follows

$$\boldsymbol{\nabla \Phi}^{MLS}(\boldsymbol{x}) = \sum_{j=1}^{n_{\boldsymbol{x}}} \boldsymbol{\nabla N}_j(\boldsymbol{x})\boldsymbol{\Phi}_j \tag{8}$$

We refer the reader to [37, 38] for complete description of the computation of the derivatives using MLS.

3.2. Phase change: relaxation algorithm

For the phase transition, the problem formulation is based on the instantaneous thermodynamical relaxation assumption [28] ($\nu \longrightarrow \infty$), obtaining a new equilibrium state (p^*,T^*,Y_1^*,Y_2^*) where the specific volume ν, the energy e and the mass fraction of the non-condensable phase Y_3 do not vary. The methodology is based on an approximation of the equilibrium mass fractions (Y_1^*,Y_2^*) rather than computing the exact solution. It is efficient and simple to implement.

In this framework, the three formulations of the vapor mass fraction are defined below,

- From the thermodynamical relation of equality between the vapor partial pressure and the saturation pressure, the vapor mass fraction Y_2^{sat} is defined as,

$$Y_2^{sat}(p, T) = \frac{p_{sat}(T)W_2}{p - p_{sat}(T)} \sum_{k=3}^{N} \frac{Y_k}{W_k}$$

- From the formulation of the mixture specific volume, the vapor mass fraction Y_2^m is defined as,

$$Y_2^m(p, T) = 1 - \frac{\nu - \nu_g(p, T)}{\nu_1(p, T) - \nu_2(p, T)} - \sum_{k=3}^{N} Y_k$$

with,

$$\nu_g(p, T) = \left(1 - \sum_{k=3}^{N} Y_k\right)\nu_2(p, T) + \sum_{k=3}^{N} Y_k \nu_k(p, T)$$

- From the formulation of the mixture energy, the vapor mass fraction Y_2^e is defined as,

$$Y_2^e(p,T) = 1 - \frac{e - e_g(p,T)}{e_1(p,T) - e_2(p,T)} - \sum_{k=3}^{N} Y_k$$

with,

$$e_g(p,T) = \left(1 - \sum_{k=3}^{N} Y_k\right) e_2(p,T) + \sum_{k=3}^{N} Y_k e_k(p,T)$$

Then, three approximations of Y_2^* are formulated,

$$\begin{cases} Y^{sat} = Y_2^m(p,T) \\ Y^m = Y_2^m(p, T_{sat}(x_v p)) \\ Y^e = Y_2^e(p, T_{sat}(x_v p)) \end{cases}$$

The strategy proposed in this method consists in the selection of the value of the approximate vapor mass fraction presented previously (Y^{sat},Y^m,Y^e) with the smallest variation, under the condition that all of them have the same sign. As described in the approach of Chiapolino et al. (2017) [35], this kind of criterion is applied by following a Minmod-type procedure. For this, a limiter parameter r is defined,

$$\begin{cases} r_1 = (Y^m - Y_2)(Y^e - Y_2) \\ r_2 = (Y^m - Y_2)(Y^{sat} - Y_2) \end{cases}$$

where Y_2 corresponds to the initial vapor mass fraction.

The vapor mass fraction is then approximated following the following criterion,

$$\begin{cases} if\ r_1 < 0\ \cup\ r_2 < 0, & Y_2^* = Y_2 \\ otherwise, & Y_2^* = Y_2 + sign(Y^m - Y_2) \times min(|Y^m - Y_2|, |Y^e - Y_2|, |Y^{sat} - Y_2|) \end{cases}$$

The new mass fraction of liquid is easily computed, since the mass fractions of the rest of the material forming the multicomponent gas are constant,

$$Y_1^* = 1 - Y_2^* - \sum_{k=3}^{N} Y_k$$

3.3. Time integration

In Equation 6, the left term is usually approximated by:

$$\int_{\Omega_I} \frac{\partial \boldsymbol{U}}{\partial t}\, d\Omega \approx \frac{\partial(\Omega_I U)}{\partial t} \tag{9}$$

In finite volume, this approximation is exact when the value at the cell center U_I is equal to the average of U on the cell. Venkatakrishnan [40] demonstrated that this approximation limit the global order of accuracy to second order. If this might not be a problem when looking for stationary solutions of a problem, it is mandatory to evaluate properly the term $\int_{\Omega_I} \frac{\partial \boldsymbol{U}}{\partial t}$ to reach higher order in unsteady simulations. In order to do that, MLS scheme is used to compute the integral of U_I on the cell volume Ω_I. Using $U(\boldsymbol{x}) \approx \sum_{j=1}^{n_x} N_j(\boldsymbol{x}) U_j$ in the integral gives:

$$\int_{\Omega_I} \frac{\partial \boldsymbol{U}}{\partial t}\, d\Omega \approx \left(\sum_{j=1}^{n_x} \int_{\Omega_I} N_j(\boldsymbol{x}) d\Omega \right) \frac{\partial \boldsymbol{U}_j}{\partial t} \tag{10}$$

Thus, the system to solve can be written as :

$$\mathbb{M}\frac{\partial \boldsymbol{U}}{\partial t} = \boldsymbol{R(U)} \tag{11}$$

With $\boldsymbol{R(U)}$ the residual vector of the system $\mathbb{M} = \left[\mu_{ij}\right]$, the mass matrix is defined by :

$$\mu_{ij} = \begin{cases} \frac{1}{\Omega_I}\int_{\Omega_I} N_j(\boldsymbol{x})d\Omega, & j \in S(i),\ stencil\ of\ \boldsymbol{x_I} \\ 0, & otherwise \end{cases} \tag{12}$$

For time stepping, a low storage fourth-order four steps Runge-Kutta is used [41].

3.4. Multi Optimal Order Detection (MOOD)

Using a high-order scheme for the discretization of equation (5) requires the use of any stabilization scheme to keep the stability of the scheme [19]. Moreover, for two-phase flow, the boundedness of the mass fraction need to be preserved [42–44].

In this work, we propose to use the Multi-dimensional Optimal Order Detection (MOOD) approach [21, 22] for the automatic local adaptation of the reconstruction order, granting the stability of the numerical scheme and the boundedness of the mass fraction.

The main idea of this approach is to compute, each step of the time integration algorithm, the cell averaged values using the most accurate available scheme. This solution is called candidate solution. Since this solution is obtained using a high-order method, it is possibly oscillating or even not physical, if negative densities and pressures appear in the solution. If this happens, this solution is not valid, which in this context means that it gives some negative densities and pressures, or that the level of nonphysical oscillations is high. A set of criteria is defined to determine if the candidate solution is valid or not. In [21] an iterative scheme was proposed for reducing progressively and locally the order of the numerical scheme, recomputing the solution and evaluating again if the solution is not admissible. This evaluation/order reduction procedure is performed until the solution is considered admissible or the numerical scheme reaches first-order, which always gives admissible solutions [21, 22]. It is worth to remark that, differently than most of the usual procedures for stabilization, the detection of the troubled cells is performed *a posteriori*, that is, once it is known the exact cells where the numerical scheme is compromised to obtain an admissible solution. The procedure is as follows. Once the candidate solution is computed each Runge-Kutta step, the following chain of detectors is used

Physical Admissible Detector (PAD)[21]: Checks if the candidate solution has positive density and pressure. Thus, if the candidate solution has negative values of pressure, density and unbounded mass fractions in a cell, or even a `NaN` value, this cell is marked as not valid and is recomputed again using a lower order scheme.

Numerical Admissible Detector (NAD) [23]: It is a relaxed version of the Discrete Maximum Principle (DMP)[21]. It checks if the solution is monotonic and new local extrema are not created.

$$\min_{\mathbf{y}\in\mathcal{V}_i}(\mathbf{U}^n(\mathbf{y})) - \delta \leqslant \mathbf{U}^*(\mathbf{x}) \leqslant \max_{\mathbf{y}\in\mathcal{V}_i}(\mathbf{U}^n(\mathbf{y})) + \delta \tag{13}$$

In equation (13) superscript n indicates the previous Runge-Kutta step, and superscript * refers to the candidate solution. The δ parameter allows a certain level of oscillations. Here we use the values proposed in [23]

$$\delta = \max\left(10^{-4}, 10^{-3}\cdot\left(\max_{\mathbf{y}\in\mathcal{V}_i}(\mathbf{U}^n(\mathbf{y})) - \min_{\mathbf{y}\in\mathcal{V}_i}(\mathbf{U}^n(\mathbf{y}))\right)\right) \tag{14}$$

Note that in order to work with this *a posteriori* formulation, all the variables in equation (14) should be normalized with an adequate reference value to get a value between 0 and 1. In the original formulation [21–23] the set $\mathcal{V}_i$ represents the set of first neighbors of the point $\mathbf{x}$. In this work the values are normalized by dividing by the maximum value in the stencil used by MLS approximations.This is based on the ideas presented in [20] in the context of slope limiters. The fulfillment of the NAD condition implies that the candidate value remains between the local minimum

and the local maximum of the previous time step. In all of the examples of this work, the NAD is checked in the density, pressure and mass fractions instead of the full vector of conservative variables, as suggested by [22].

The whole procedure is presented schematically on Figure 1.

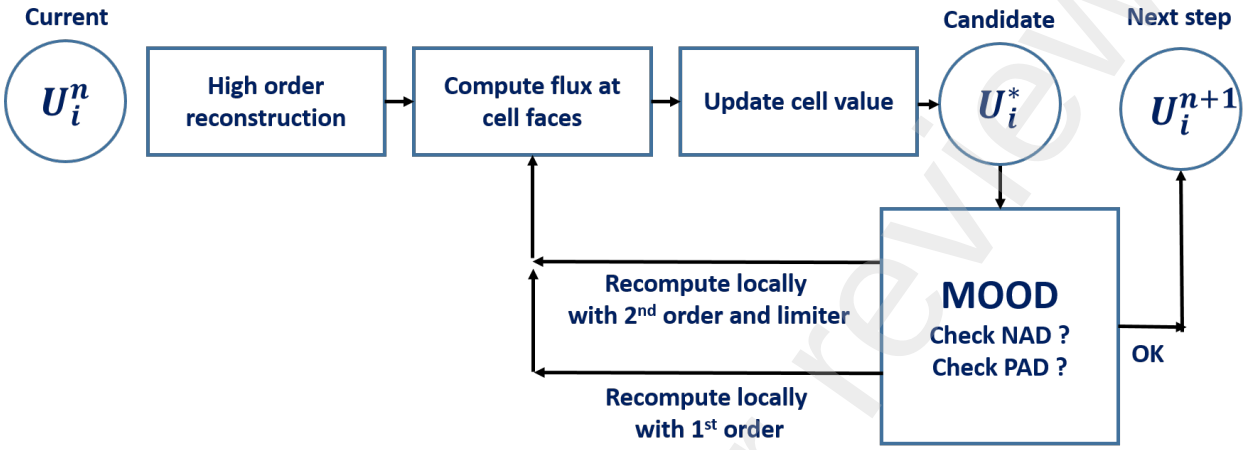

Figure 1: MOOD algorithm

3.5. *Interface advection test*

This first test case is designed to demonstrate the ability of the proposed numerical method to handle arbitrary order of accuracy. For this purpose, a scalar transport problem is simulated on various meshes. The transported scalar is the mass fraction Y_1. It is advected at constant speed $u = 100m.s^{-1}$ and constant pressure. At $t = 0$, the interface is initialized using an hyperbolic tangent as a transition function (eq 15,16 and 17).

$$Y_1(x) = 0.9 \times g_1 + 0.1 \times g_2 \tag{15}$$

With

$$g_1 = 0.5 \times \left[1.0 + tanh\frac{x_0 - x}{b}\right] \tag{16}$$

$$g_2 = 0.5 \times \left[1.0 + tanh\frac{x - x_0}{b}\right] \tag{17}$$

The domain is [-0.5m,0.5m]x[-0.05m,0.05m]. The initial conditions are set with $x_0 = -0.25m$ and $b = 0.01m$ and presented in Figure 2 on triangular mesh of $0.01m$ base size.

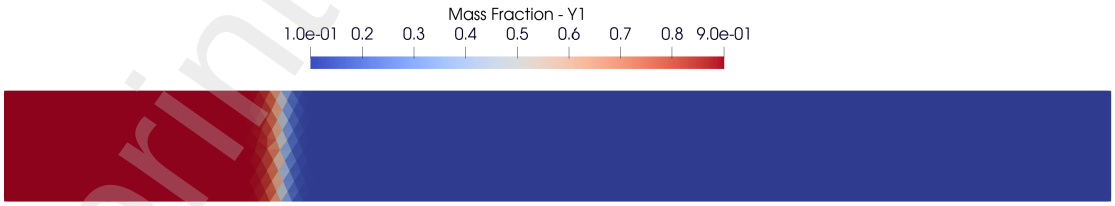

Figure 2: Initial conditions for the advection test case

Figure 3 shows the evolution of the advected interface for different time instants, for a cut at $y = 0$, and also a comparison between the the analytical solution and the solution obtained for different third-order schemes on the same mesh. Figure 3 (a) shows the numerical solutions using a third-order Finite Volume Method without any stabilization procedure. It is noticed the numerical oscillations in the solution, having under and overshoots, which are not physical. These oscillations would lead to unbounded solution for the mass fraction if the test was carried out with mass fraction

ranging from 0 to 1. Figure 3 (b) shows the results using the Barth and Jespersen limiter [45]. It is observed that the oscillations are removed, but at the cost of introducing excessive numerical dissipation. Figure 3 (c) show the results using the proposed approach with the MOOD procedure. It is noticed that the numerical oscillations are prevented, but also the interface is kept sharp, which is related to a lower numerical dissipation in comparison with Figure 3 (b).

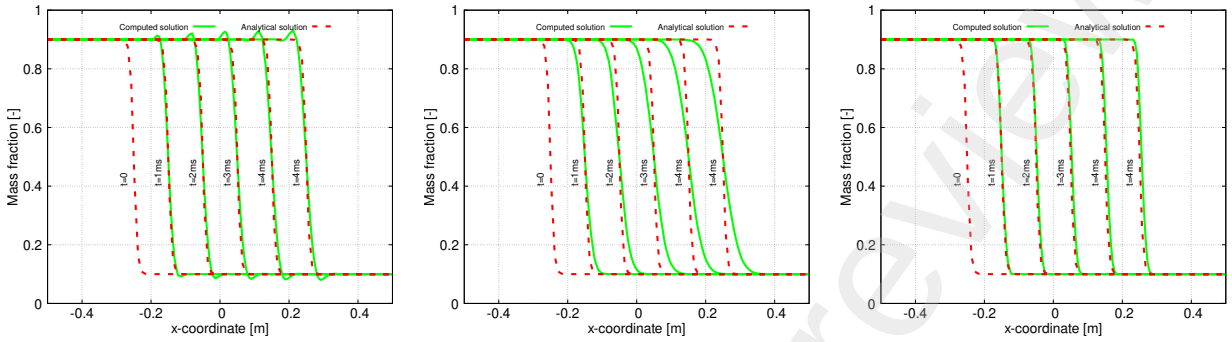

(a) Without limiter, without MOOD

(b) With limiter, without MOOD

(c) Without limiter, with MOOD

Figure 3: Interface advection test: Comparison between the numerical solution at $y = 0$ using different limiting procedures with the analytical solution for different time instants.

Figure 4 shows the evolution of the L_2 error versus the mesh size using the proposed approach. As expected, the targeted orders of accuracy from 3 to 6 are well recovered.

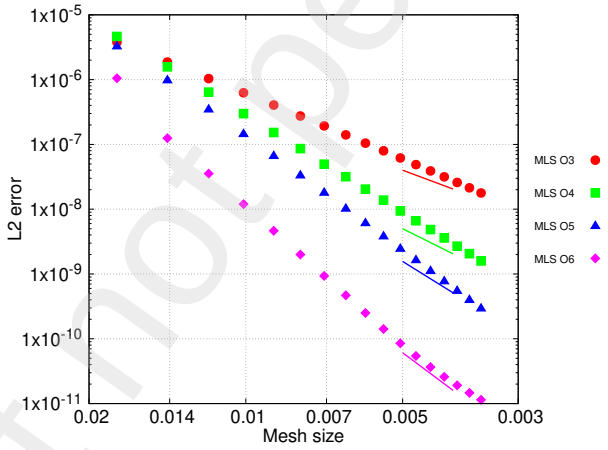

Figure 4: L2 error versus mesh size for various orders of accuracy using the proposed approach. The lines are the slopes corresponding to the targeted orders.

3.6. Shock tube tests with phase change

Four shock tube test cases are carried out demonstrating the ability of the proposed solver to deal with stiff thermodynamic two-phase flow problems with phase transition as presented in [28]. The four test cases described below are carried out in 2D on a 1mx0.1m shock tube with a regular triangular mesh of 0.01m base size, similar to the one presented in Figure 2. Although our simulations are carried out in 2D, we used the same resolution (100 points along x-axis) as in Chaipolino et al in [28].

1. Pressure shock with a mixture far from the phase bounds
2. Pressure shock with a mixture of air and 2% of steam
3. Pressure shock with a mixture mainly made of liquid water

4. Double expansion with a mixture mainly made of liquid water

The parameters for the NASG equation of state for the four test cases are presented in Table 1

Coefficient	Liquid phase (Water)	Vapor phase (Steam)	Non cond. phase (air)
γ	1.19	1.47	1.4
$P_\infty\ (Pa)$	7.028×10^4	0.0	
$c_v\ (J/kg/K)$	3610.0	955.0	719.0
$b\ (m3/kg)$	$6.61 \times 10^{-}4$	0.0	
$q\ (J/kg)$	-1177788.0	2077616.0	
$q'\ (J/kg/K)$	0.0	14317.0	
$W\ (g/mol)$	18.0		29.0

Table 1: Parameters for NASG EOS for water/steam/air from [35]

A comparison with the results obtained in [35]using a 2nd order MUSCL Hancock method using van Leer's slope limiter are presented in Figure 5, Figure 6, Figure 7 and Figure 8. The obtained results are in good agreement with the reference [35]. It can also be notice that the proposed scheme allows to capture sharper shocks for case 1 to 3 without any numerical instabilities.

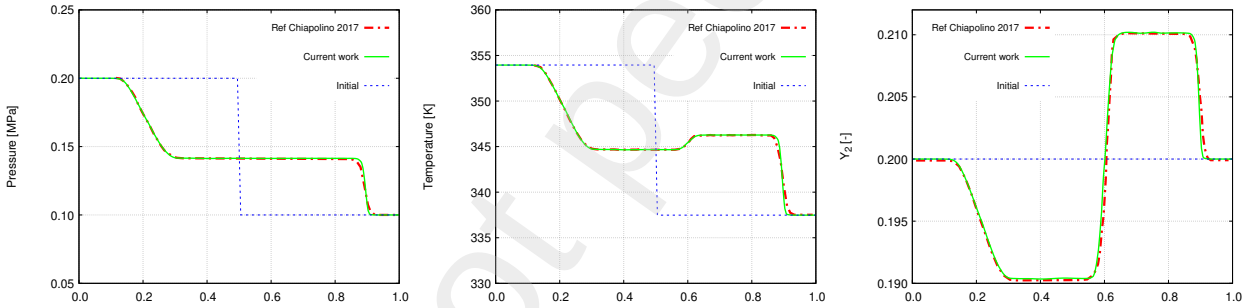

(a) Pressure (b) Temperature (c) Steam mass fraction

Figure 5: Comparison between the proposed scheme and the results of Chiapolino [28]. Pressure discontinuity inside a shock tube containing 10% water, 20% steam and 70% of air in mass fractions

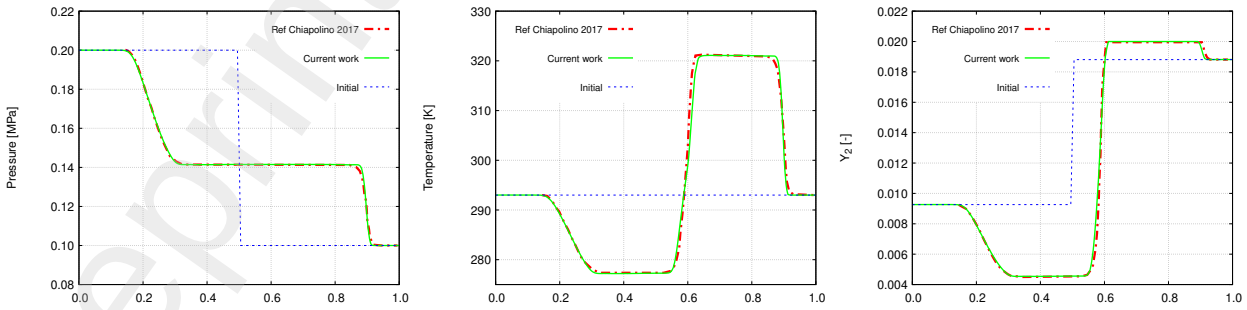

(a) Pressure (b) Temperature (c) Steam mass fraction

Figure 6: Comparison between the proposed scheme and the results of Chiapolino [28]. Pressure discontinuity inside a shock tube containing 98% of air and 2% of steam in mass fractions

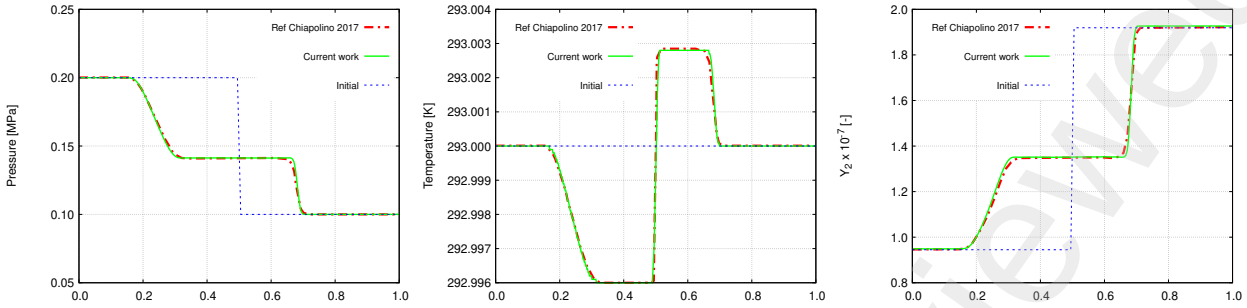

(a) Pressure (b) Temperature (c) Steam mass fraction

Figure 7: Comparison between the proposed scheme and the results of Chiapolino [28]. Pressure discontinuity inside a shock tube containing mainly liquid water with only 10^{-5} of air in mass fractions

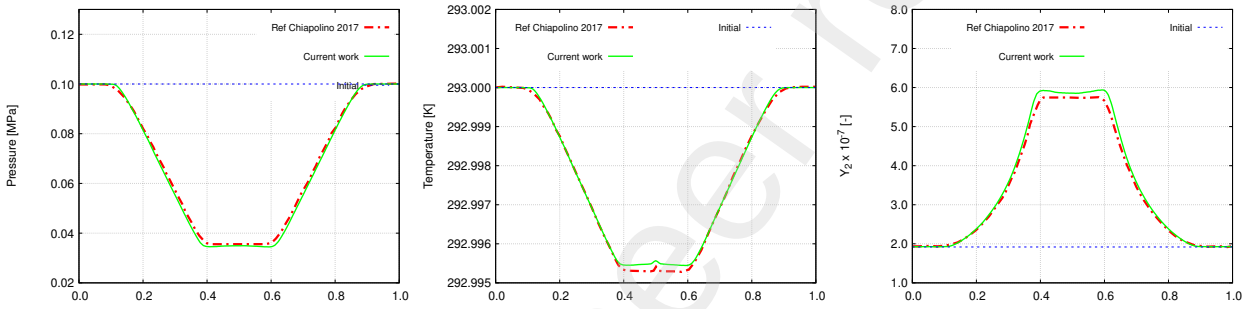

(a) Pressure (b) Temperature (c) Steam mass fraction

Figure 8: Comparison between the proposed scheme and the results of Chiapolino [28]. Velocity discontinuity inside a shock tube containing mainly liquid water with only 10^{-5} of air in mass fractions

3.7. Shock interaction with a Helium bubble

Another classical test case for the validation of two-phase flow solver is the interaction between a shock and a helium bubble. The perfect ideal gas equation of state are recovered using the parameters in Table 2 for NASG, where the first phase usually considered as a liquid the aire and the second phase, as well as the non-condensable phase have the parameters for helium gas.

Coefficient	Liquid phase	Vapor phase	Non cond. phase
γ	1.4	1.66	1.66
P_∞ (Pa)	0.0	0.0	0.0
c_v $(J/kg/K)$	719.0	3120.871	3120.871
b $(m3/kg)$	0.0	0.0	0.0
q (J/kg)	0.0	0.0	0.0
q' $(J/kg/K)$	0.0	0.0	0.0
W (g/mol)	29.0	4.0	

Table 2: Shock interaction with a Helium bubble: Parameters for NASG EOS for air/helium.

In this test case, Y_1 is the mass fraction of air, Y_2 the mass fraction of helium. The relaxation algorithm for phase transition is deactivated. The remaining mass fraction Y_3 is initialized at 0 and remains equal to 0 throughout the simulation. The bubble contour and the pressure of the shock are initialized with a Heaviside jump as sharp interface. We note that as an improvement from our previous work, [44], it is not anymore necessary to initialize the domain using smooth hyperbolic tangent smooth transition. With the proposed formulation, strict jump in mass fraction for

the bubble and pressure for the shock are handled perfectly without oscillation while preserving boundedness. We used a regular triangle mesh with a base size of 0.416mm. The computational domain has then a total number of cells of 311,630 triangles. The setup of this test case is schematically described in Figure 9.

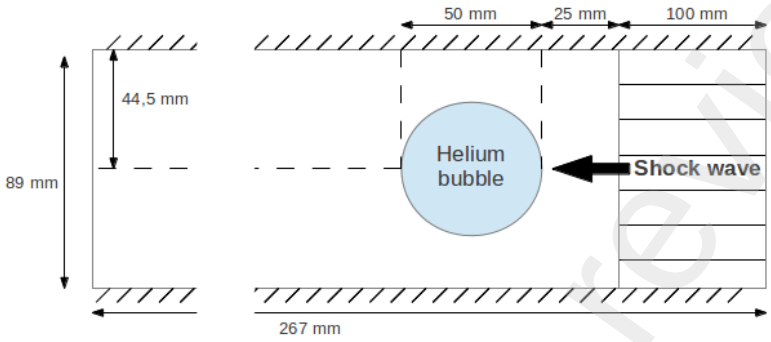

Figure 9: Shock interaction with a Helium bubble. Description of the test case

The density field and mass fraction field at $t = 437\mu s$ after the shock are presented respectively in Figure 10. At this time, the cells where PAD and NAD were activated are presented in Figure 11. It is noticed that even in this coarse mesh, the proposed scheme is able to capture the Ritchmyer-Meshkov instabilities at the interface. As it can be seen in Figure 11, most of the domain is using the third-order scheme. Moreover, the solution keeps the symmetry, and no numerical artifacts are observed.

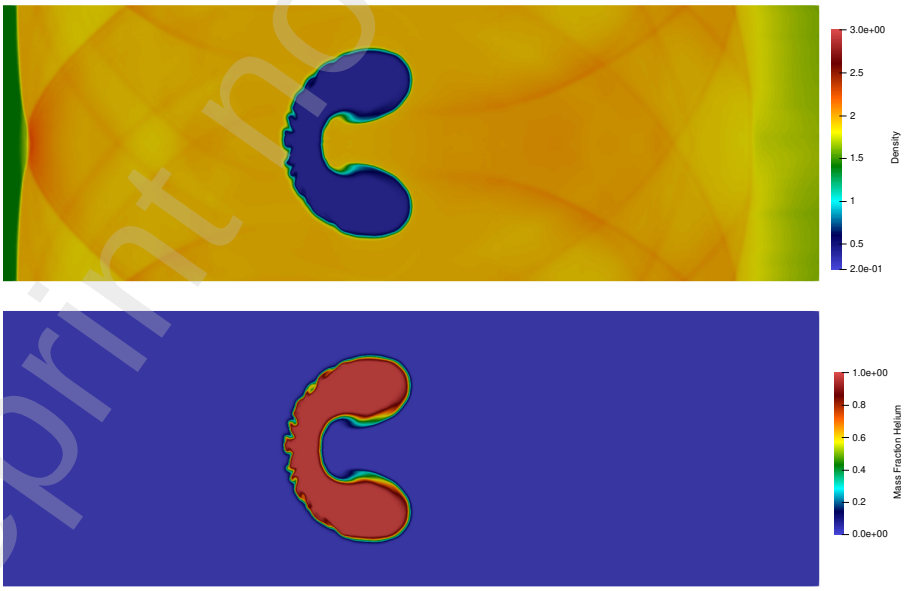

Figure 10: Shock interaction with a Helium bubble, $437\mu s$ after the hitting shock. Density field (top) and Mass fraction field of helium (bottom)

Figure 11: Shock interaction with a Helium bubble, 437μs after the hitting shock. NAD activation map (top) and PAD activation map (bottom)

The time evolution of the interfaces (upstream, downstream and jet) are presented in Figure 12. The results are in very good agreement with the results presented in [46] and [47].

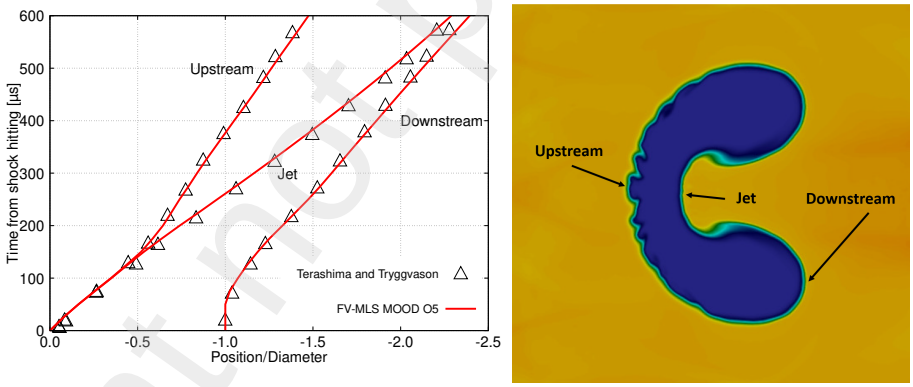

Figure 12: Time histories of the interfaces position obtained with FV-MLS+MOOD and comparison with the computational results from [46]

3.8. Evaporating liquid jet

Finally, we illustrate the robustness and accuracy of our computational framework through a demonstrative test case: the simulation of a liquid oxygen jet in a gaseous hydrogen flow presented in Figure 13. This test, inspired by the setup proposed in [35], aims to show the ability of the proposed method to handle complex, multiphase flow problems on a coarse mesh. The mesh presented in Figure 14 has 29410 triangles. At the interface between the jets and the domain (axis to point F), the mesh size is 0.4mm. It has growth rate of 1.01 with a maximum size of 1mm in the left side. On the right side, the growth rate is 1.1 with a maximum size of 2mm.

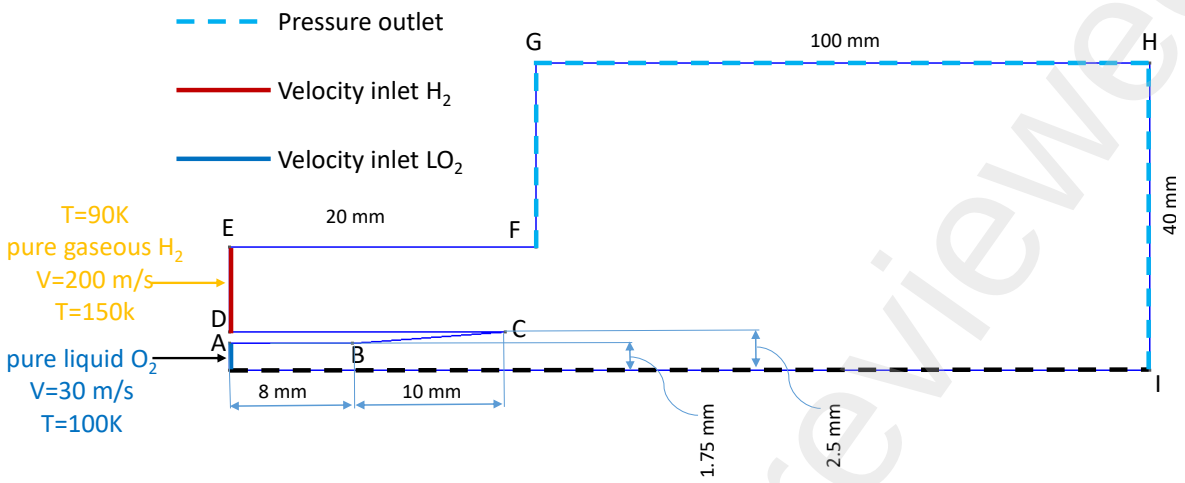

Figure 13: Test case definition for liquid O_2 jet in gaseous H_2 flow. Only half domain is represented. The black dashed line is a symmetry plane.

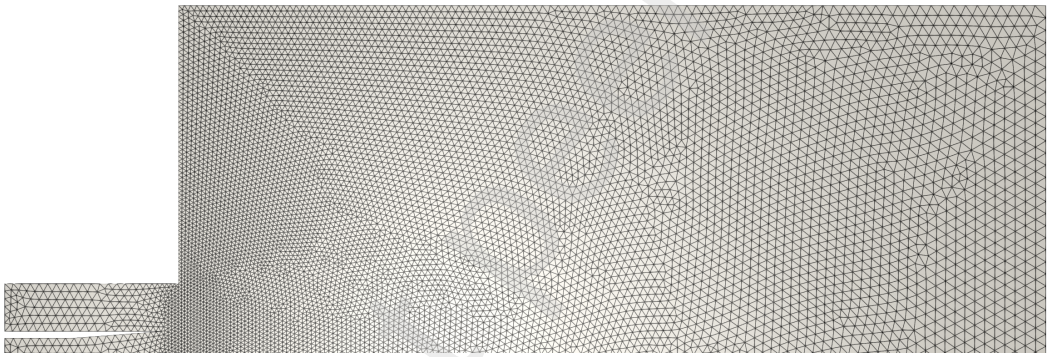

Figure 14: Overview of the mesh used for the simulations - top half of the domain

The boundary conditions are defined as

- Central jet: pure liquid O_2, $Y_1 = 1.0$, $V_x = 30m/s$, $T = 100K$
- Peripheral flow: pure gaseous H_2, $Y_3 = 0.0$, $V_x = 200m/s$, $T = 150$
- Pressure outlet: $P = 3\ MPa$

The parameter for NASG EOS are summarized in Table 3.

Coefficient	Liquid phase (O_2)	Vapor phase (O_2)	Non cond. phase (H_2)
γ	2.45	1.47	1.4
$P_\infty\ (Pa)$	1.062×10^8	0.0	
$c_v\ (J/kg/K)$	695.0	531.0	10183.0
$b\ (m3/kg)$	6.61×10^{-4}	0.0	
$q\ (J/kg)$	-2.58×10^5	6.9×10^3	-1.2×10^6
$q'\ (J/kg/K)$	0.0	-9.28×10^3	
$W\ (g/mol)$	18.0		29.0

Table 3: Parameters for NASG EOS for liquid O2/ gaseous O2 /non condensable H2 from [35]

Figure 15 shows the O2 gas mass fraction that has evaporation at the jet interface. Figure 16 presents the mass fraction of hydrogen non condensable phase. Figure 17 and Figure 18 the cells activated by the PAD detector and the NAD detector are highlighted in red.

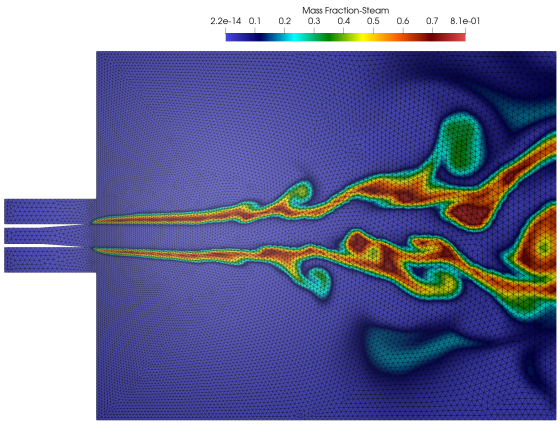

Figure 15: Liquid O_2 jet in H_2 gas - O_2 gas mass fraction - with view of the mesh

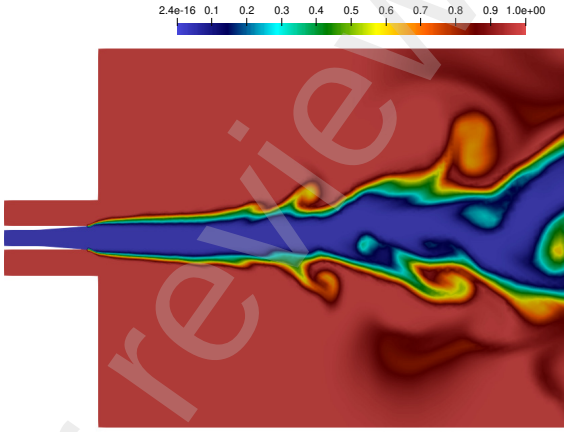

Figure 16: Liquid O_2 jet in H_2 gas - H_2 gas mass fraction

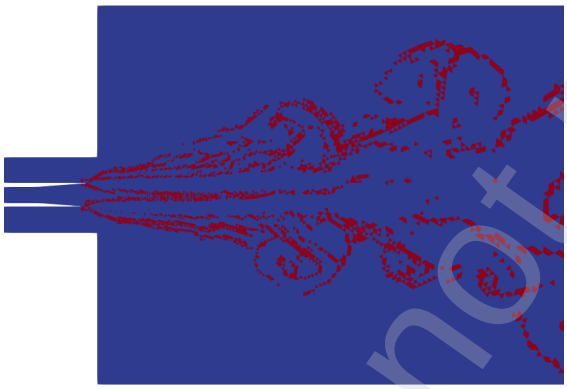

Figure 17: Liquid O_2 jet in H_2 gas - cells where PAD is activated

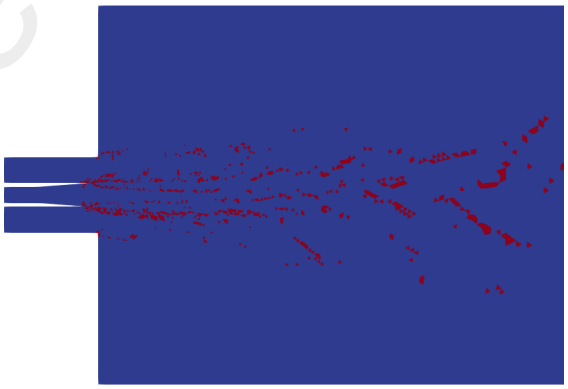

Figure 18: Liquid O_2 jet in H_2 gas - cells where NAD is activated

A notable feature of the proposed solver is its ability to maintain sharp interfaces between the phases. This is crucial for accurately modeling the inherent jet instabilities, a challenging aspect that the proposed method successfully reproduces. The results validate our methodology for the simulation of complex scenarios, and seems to indicate its potential for conducting implicit Large Eddy Simulations (iLES). The accurate prediction of jet instabilities, along with the preservation of sharp phase interfaces, even on a coarse mesh, underscores the applicability of the proposed method to real-world fluid dynamics problems.

Conclusions

In this paper, we addressed the simulation problem of multi-component two-phase flows with phase transitions on an unstructured mesh using a diffuse interface. The solver relies on the Homogeneous Relaxation Model (HRM) and the Noble-Abel Stiffened Gas (NASG) Equation of State proposed by Saurel et al. [27] and further developed by Chiapolino et al. [28]. The proposed approach combines the finite volume method with high-order reconstruction

based on moving least squares reproducing kernels. The numerical instabilities that typically appear when using high-order reconstruction in areas with strong gradients and shocks are prevented through the adoption of the Multi Optimal Order Detection (MOOD) approach. It adjusts the reconstruction order *a posteriori* to maintain the highest accuracy while preventing numerical oscillations and non-physical values. A novel phase change algorithm is also presented.

We have demonstrated the capability of the proposed method to address the simulation of complex multi-component two-phase flows through several numerical examples: the simple interface advection test, four shock tube tests with phase change, the shock interaction with a Helium bubble and the evaporating liquid jet. The results shows that our scheme is robust, accurate, preserves sharp interfaces and is able to handle complex flow scenarios, even on coarse meshes. Future work will focus on combining this approach with implicit Large Eddy Simulation (iLES) techniques to study turbulent two-phase flow with heat and mass transfer.

Acknowledgements

X. Nogueira and L. Ramírez acknowledge the support provided by the [Grant PID2021-125447OB-I00] funded by MCIN/AEI/ 10.13039/501100011033 and by "ERDF A way of making Europe", and the funds by [Grant TED2021-129805B-I00] funded by MCIN/AEI/ 10.13039/501100011033 and by the "European Union NextGenerationEU/PRTR". They also acknowledge the funding provided by the Xunta de Galicia (grant #ED431C 2022/06).

LIFSE laboratory gratefully acknowledges the funding of the PhD work of Carlos Romero-Casado from the Ariane Group and the Agence Nationale de la Recherche Technologique.

References

[1] S. Le Martelot, R. Saurel, B. Nkonga, Towards the direct numerical simulation of nucleate boiling flows, International Journal of Multiphase Flow 66 (2014) 62–78. doi:https://doi.org/10.1016/j.ijmultiphaseflow.2014.06.010.

[2] Y. Lv, J. Ekaterinaris, Recent progress on high-order discontinuous schemes for simulations of multiphase and multicomponent flows, Progress in Aerospace Sciences 140 (2023) 100929. doi:10.1016/j.paerosci.2023.100929.

[3] M. De Lorenzo, P. Lafon, M. Pelanti, A. Pantano, M. Di Matteo, Y. Bartosiewicz, J. M. Seynhaeve, A hyperbolic phase-transition model coupled to tabulated EoS for two-phase flows in fast depressurizations, Nuclear Engineering and Design 371 (2021) 110954. doi:10.1016/j.nucengdes.2020.110954.

[4] H. Xu, A. F. Badea, X. Cheng, Analysis of two phase critical flow with a non-equilibrium model, Nuclear Engineering and Design 372 (372) (2021) 110998. doi:10.1016/j.nucengdes.2020.110998.

[5] A. Majumdar, A. LeClair, J. Hartwig, S. Mostafa Ghiaasiaan, Numerical modeling of no vent filling of a cryogenic tank with thermodynamic vent system augmented injector, Cryogenics 131 (2023) 103651. doi:10.1016/j.cryogenics.2023.103651.

[6] F. Huerta, V. Vesovic, CFD modelling of the non-isobaric evaporation of cryogenic liquids in storage tanks, Applied Energy 356 (2024) 122420. doi:10.1016/j.apenergy.2023.122420.

[7] A. Romei, G. Persico, Computational fluid-dynamic modelling of two-phase compressible flows of carbon dioxide in supercritical conditions, Applied Thermal Engineering 190 (2021) 116816. doi:10.1016/j.applthermaleng.2021.116816.

[8] A. Krimi, L. Ramírez, S. Khelladi, F. Navarrina, M. Deligant, X. Nogueira, Improved δ-sph scheme with automatic and adaptive numerical dissipation, Water (Switzerland) 12 (10) (2020). doi:10.3390/w12102858.

[9] A. Krimi, M. Rezoug, S. Khelladi, X. Nogueira, M. Deligant, L. Ramírez, Smoothed Particle Hydrodynamics: A consistent model for interfacial multiphase fluid flow simulations, Journal of Computational Physics 358 (2018) 53 – 87. doi:10.1016/j.jcp.2017.12.006.

[10] I. Hammani, S. Marrone, A. Colagrossi, G. Oger, D. Le Touzé, Detailed study on the extension of the δ-SPH model to multi-phase flow, Computer Methods in Applied Mechanics and Engineering 368 (2020) 113189. doi:https://doi.org/10.1016/j.cma.2020.113189.

[11] C. S. From, E. Sauret, S. A. Galindo-Torres, Y. T. Gu, Interaction pressure tensor on high-order lattice Boltzmann models for nonideal fluids, Physical Review E 99 (6) (2019) 1–20. doi:10.1103/PhysRevE.99.063318.

[12] Q. Li, K. H. Luo, Q. J. Kang, Y. L. He, Q. Chen, Q. Liu, Lattice Boltzmann methods for multiphase flow and phase-change heat transfer, Progress in Energy and Combustion Science 52 (2016) 62–105. doi:10.1016/j.pecs.2015.10.001.

[13] M. Specklin, P. Dubois, A. Albadawi, Y. M. C. Delauré, A full immersed boundary solution coupled to a Lattice–Boltzmann solver for multiple fluid–structure interactions in turbulent rotating flows, Journal of Fluids and Structures 90 (2019) 205–229. doi:10.1016/j.jfluidstructs.2019.06.014.

[14] D. W. Schwendeman, C. W. Wahle, a.K. Kapila, a. Kapila, The Riemann problem and a high-resolution Godunov method for a model of compressible two-phase flow, Journal of Computational Physics 212 (2) (2006) 490–526. doi:10.1016/j.jcp.2005.07.012.

[15] C. T. Ha, W. G. Park, C. M. Jung, Numerical simulations of compressible flows using multi-fluid models, International Journal of Multiphase Flow 74 (2015) 5–18. doi:10.1016/j.ijmultiphaseflow.2015.03.022.

[16] Y. Sato, B. Ničeno, A sharp-interface phase change model for a mass-conservative interface tracking method, Journal of Computational Physics 249 (2013) 127–161. doi:10.1016/j.jcp.2013.04.035.

[17] T. Nonomura, K. Kitamura, K. Fujii, A simple interface sharpening technique with a hyperbolic tangent function applied to compressible two-fluid modeling, Journal of Computational Physics 258 (2014) 95–117. doi:10.1016/j.jcp.2013.10.021.

[18] C. Foulquié, S. Khelladi, M. Deligant, L. Ramírez, X. Nogueira, J. Mardjono, Numerical assessment of fan blades screen effect on fan/OGV interaction tonal noise, Journal of Sound and Vibration 481 (2020). doi:https://doi.org/10.1016/j.jsv.2020.115428.
[19] K. Michalak, C. Ollivier-Gooch, Limiters for unstructured higher-order accurate solutions of the Euler equations, 46th AIAA Aerospace Sciences Meeting and Exhibit (2008) 1–14doi:https://doi.org/10.2514/6.2008-776.
[20] P. Tsoutsanis, Extended bounds limiter for high-order finite-volume schemes on unstructured meshes, Journal of Computational Physics 362 (2018) 69–94. doi:10.1016/j.jcp.2018.02.009.
[21] S. Clain, S. Diot, R. Loubère, A high-order finite volume method for systems of conservation laws-Multi-dimensional Optimal Order Detection (MOOD), Journal of Computational Physics (10) (2011) 4028–4050. doi:10.1016/j.jcp.2011.02.026.
[22] S. Diot, S. Clain, R. Loubère, Improved detection criteria for the Multi-dimensional Optimal Order Detection (MOOD) on unstructured meshes with very high-order polynomials, Computers and Fluids 64 (2012) 43–63. doi:10.1016/j.compfluid.2012.05.004.
[23] R. Loubère, M. Dumbser, S. Diot, A new family of high order unstructured mood and ader finite volume schemes for multidimensional systems of hyperbolic conservation laws, Communications in Computational Physics 16 (3) (2014) 718–763. doi:10.4208/cicp.181113.140314a.
[24] B. Boyd, D. Jarrahbashi, A diffuse-interface method for reducing spurious pressure oscillations in multicomponent transcritical flow simulations, Computers and Fluids 222 (2021) 104924. doi:https://doi.org/10.1016/j.compfluid.2021.104924.
[25] M. Pelanti, Low Mach number preconditioning techniques for Roe-type and HLLC-type methods for a two-phase compressible flow model, Applied Mathematics and Computation 310 (2017) 112–133. doi:https://doi.org/10.1016/j.amc.2017.04.014.
[26] X. Nogueira, L. Ramírez, S. Khelladi, J.-C. Chassaing, I. Colominas, A high-order density-based finite volume method for the computation of all-speed flows, Computer Methods in Applied Mechanics and Engineering 298 (2016) 229 – 251. doi:https://doi.org/10.1016/j.cma.2015.10.004.
[27] R. Saurel, P. Boivin, O. Le Métayer, A general formulation for cavitating, boiling and evaporating flows, Computers & Fluids 128 (2016) 53–64. doi:https://doi.org/10.1016/j.compfluid.2017.03.022.
[28] A. Chiapolino, P. Boivin, R. Saurel, A simple and fast phase transition relaxation solver for compressible multicomponent two-phase flows, Computers & Fluids 150 (2017) 31–45. doi:https://doi.org/10.1016/j.compfluid.2017.03.022.
[29] O. Le Métayer, R. Saurel, The noble-abel stiffened-gas equation of state, Physics of Fluids 28 (4) (2016) 046102. doi:https://doi.org/10.1063/1.4945981.
[30] A. Chiapolino, R. Saurel, Extended noble-Abel stiffened-gas equation of state for sub-and-supercritical liquid-gas systems far from the critical point, Fluids 3 (3) (2018). doi:https://doi.org/10.3390/fluids3030048.
[31] R. Saurel, F. Petitpas, R. Abgrall, Modelling phase transition in metastable liquids: application to cavitating and flashing flows, Journal of Fluid Mechanics 607 (2008) 313–350. doi:10.1017/S0022112008002061.
[32] E. F. Toro, M. Spruce, W. Speares, Restoration of the contact surface in the hll-riemann solver, Shock waves 4 (1) (1994) 25–34. doi:https://doi.org/10.1007/BF01414629.
[33] S. Tokareva, E. F. Toro, Hllc-type riemann solver for the baer–nunziato equations of compressible two-phase flow, Journal of Computational Physics 229 (10) (2010) 3573–3604. doi:https://doi.org/10.1016/j.jcp.2010.01.016.
[34] S. Le Martelot, R. Saurel, B. Nkonga, Towards the direct numerical simulation of nucleate boiling flows, International Journal of Multiphase Flow 66 (2014) 62–78. doi:https://doi.org/10.1016/j.ijmultiphaseflow.2014.06.010.
[35] A. Chiapolino, P. Boivin, R. Saurel, A simple phase transition relaxation solver for liquid–vapor flows, International Journal for Numerical Methods in Fluids 83 (7) (2017) 583–605. doi:https://doi.org/10.1002/fld.4282.
[36] L. Cueto-Felgueroso, I. Colominas, J. Fe, F. Navarrina, M. Casteleiro, High-order finite volume schemes on unstructured grids using moving least-squares reconstruction. Application to shallow water dynamics, International Journal for Numerical Methods in Engineering 65 (3) (2006) 295–331. doi:10.1002/nme.1442.
[37] L. Cueto-Felgueroso, I. Colominas, X. Nogueira, F. Navarrina, M. Casteleiro, Finite volume solvers and moving least-squares approximations for the compressible navier–stokes equations on unstructured grids, Computer Methods in Applied Mechanics and Engineering 196 (45) (2007) 4712 – 4736. doi:https://doi.org/10.1016/j.cma.2007.06.003.
[38] S. Khelladi, X. Nogueira, F. Bakir, I. Colominas, Toward a higher order unsteady finite volume solver based on reproducing kernel methods, Computer Methods in Applied Mechanics and Engineering 200 (29-32) (2011) 2348–2362. doi:10.1016/j.cma.2011.04.001.
[39] X. Nogueira, I. Colominas, L. Cueto-Felgueroso, S. Khelladi, On the simulation of wave propagation with a higher-order finite volume scheme based on reproducing kernel methods, Computer Methods in Applied Mechanics and Engineering 199 (23) (2010) 1471 – 1490. doi:https://doi.org/10.1016/j.cma.2009.12.015.
URL http://www.sciencedirect.com/science/article/pii/S0045782509004216
[40] V. Venkatakrishnan, D. J. Mavriplis, Implicit Method for the Computation of Unsteady Flows on Unstructured Grids, 12th Computational Fluid Dynamics Conferencedoi:doi.org/10.2514/6.1995-1705,year={1995}.
[41] C. A. Kennedy, M. H. Carpenter, R. M. Lewis, Low-storage, explicit Runge-Kutta schemes for the compressible Navier-Stokes equations, Applied Numerical Mathematics 35 (3) (2000) 177–219. doi:10.1016/S0168-9274(99)00141-5.
[42] H. Jasak, H. G. Weller, A. D. Gosman, High resolution NVD differencing scheme for arbitrarily unstructured meshes, International journal for numerical methods in fluids 449 (31) (1999) 431–449. doi:doi.org/10.1002/(SICI)1097-0363(19990930)31:2<431::AID-FLD884>3.0.CO;2-T.
[43] M. Herrmann, G. Blanquart, V. Raman, Flux corrected finite-volume scheme for preserving scalar boundedness in large-eddy simulations, Annu. Res. Briefs (2004) 10–13doi:10.2514/6.2005-1282.
[44] M. Deligant, M. Specklin, S. Khelladi, A naturally anti-diffusive compressible two phases Kapila model with boundedness preservation coupled to a high order finite volume solver, Computers & Fluids 114 (2015) 265–273. doi:10.1016/j.compfluid.2015.03.004.
[45] T. J. Barth, D. C. Jespersen, The design and application of upwind schemes on unstructured meshes, in: 27th Aerospace Sciences Meeting AIAA-89-0366, 1989. doi:10.2514/6.1989-366.
[46] H. Terashima, G. Tryggvason, A front-tracking/ghost-fluid method for fluid interfaces in compressible flows, Journal of Computational Physics 228 (11) (2009) 4012–4037. doi:https://doi.org/10.1016/j.jcp.2009.02.023.

[47] P. Tsoutsanis, M. S. S. Pavan Kumar, P. S. Farmakis, A relaxed a posteriori MOOD algorithm for multicomponent compressible flows using high-order finite-volume methods on unstructured meshes, Applied Mathematics and Computation 437 (2023) 127544. doi:10.1016/j.amc.2022.127544.